Research Square

Preprints are preliminary reports that have not undergone peer review.
They should not be considered conclusive, used to inform clinical practice,
or referenced by the media as validated information.

Lightweight MXene–B_4C–Polyimide Nanocomposite for Simultaneous Cosmic Radiation and Electromagnetic Interference Shielding in Aerospace Avionics

Elhan Ayath

s21511007116@nu.ac.bd

CATECH, National University

Arshad Adam Salema

Monash University

Saidur Rahman

Sunway University

Md. Abu Zaed

Sunway University

Mohammad Zahangir Alam

University of Turku

Article

Keywords: SRIM/TRIM, Single-Event-Upsets, Solar-flux, Solar-flare, Solar system, Space Radiation

Posted Date: November 12th, 2026

DOI: https://doi.org/10.21203/rs.3.rs-10946351/v1

License: This work is licensed under a Creative Commons Attribution 4.0 International License.
Read Full License

Additional Declarations: No competing interests reported.

Lightweight MXene–B_4C–Polyimide Nanocomposite for Simultaneous Cosmic Radiation and Electromagnetic Interference Shielding in Aerospace Avionics

Elhan Ayath[1[0009-0003-8411-6552]], Arshad Adam Salema[2[0000-0003-2924-6680]], Saidur Rahman[3[0000-0002-2656-3034]], Md. Abu Zaed[3[0000-0001-8788-4635]], and Mohammad Zahangir Alam[4[0009-0009-0130-339X]]

[1]Department of Aerospace and Aviation Science, CATECH, National University, Bangladesh
s21511007116@nu.ac.bd
[2]Department of Mechanical Engineering, Monash University, Malaysia
Arshad.salema@monash.edu
[3]Faculty of Engineering and Technology, Sunway University, Malaysia
saidur@sunway.edu.my
[3] Faculty of Engineering and Technology, Sunway University, Malaysia
abuz@sunway.edu.my
[4]Department of Computing, ML and Software Engineering, University of Turku, Finland
mohammad.z.alam@utu.fi

Abstract. At cruise altitudes, atmospheric proton radiation and electromagnetic interference (EMI) jointly threaten the reliability of flight-critical avionics. Conventional protection strategies typically address these hazards separately through aluminum- or lead-based radiation barriers and conductive copper-mesh EMI shields, increasing enclosure mass, volume, and integration complexity. To address this limitation, we present a lightweight dual-function MXene ($Ti_3C_2T_x$)–B_4C–polyimide nanocomposite that combines proton attenuation and EMI shielding within a single conformal material system. The framework integrates SRIM/TRIM-guided compositional design, controlled nanocomposite fabrication, proton-beam testing, broadband EMI characterization, and aerospace-relevant environmental validation. SRIM/TRIM simulations show that a boron-rich composition of 31 at% achieves complete stopping of 50 MeV protons at approximately 36 mm bulk thickness, with electronic stopping dominating energy loss and negligible backscattering. Surface-functionalized B_4C nanoparticles (~45 nm) and exfoliated MXene nanosheets are incorporated through solution casting and vacuum-assisted filtration. At 20 wt% B_4C and 15 wt% MXene, the 36 mm composite achieves 100% proton attenuation, approximately fivefold higher than an aerospace-grade aluminum reference, and 54.7 dB EMI shielding across the X-band (8.2–12.4 GHz). Electrical conductivity reaches 2.1×10^4 S/m, flexibility is retained to a 2 mm bend radius, and areal mass is reduced by ~81% relative to a 2.0 mm aluminum reference. Selected RTCA DO-160G-aligned tests confirm performance retention after 500 thermal cycles and 1,000 h humidity exposure. MCNP6.2 simulations further project an eightfold reduction in processor radiation dose. Overall, the optimized composition balances proton attenuation, EMI shielding, flexibility, and mass efficiency within aerospace-relevant thickness constraints, supporting lightweight multifunctional protection for aerospace electronics.

Keywords: SRIM/TRIM, Single-Event-Upsets, Solar-flux, Solar-flare, Solar system, Space Radiation.

1 Introduction

Modern aircraft operate in an environment where reliability is not merely a design objective but a safety imperative. As avionics systems evolve toward higher computational density, greater connectivity, and tighter subsystem integration, they are increasingly exposed to multiple environmental stressors at cruise altitude [1], [2]. Among the most critical are ionizing radiation and electromagnetic interference (EMI), which represent concurrent but physically distinct threats to flight-critical electronics [1]–[3]. Radiation can induce single-event effects and cumulative degradation in semiconductor devices [1], [2], whereas EMI can compromise signal integrity and disrupt communication, navigation, and control pathways [3]. In highly integrated avionics architectures, disturbances from either domain may propagate through shared computational and communication infrastructure, motivating lightweight protection strategies capable of addressing both hazards within a unified material system.

At typical commercial flight altitudes of 35,000–40,000 ft, the atmospheric radiation environment is substantially more intense than at sea level, with elevated fluxes of high-energy protons, secondary neutrons, and other particles that increase the probability of radiation-induced faults in sensitive electronic components [4], [5]. These interactions can produce single-event upsets (SEUs), transient errors, data corruption, and cumulative hardware degradation [1], [2], [5]. Although radiation-hardened devices and fault-tolerant architectures can reduce these risks, material-based shielding remains an important complementary strategy, particularly where weight, cost, power, and integration constraints limit extensive hardware redundancy.

Concurrently, increasing use of high-speed processors, advanced data buses, satellite communication links, radar, and high-power radiofrequency subsystems has intensified EMI concerns. EMI can disrupt communication, navigation, and flight-control electronics and degrade signal integrity [3], [6]. These risks are particularly relevant in integrated modular avionics architectures, where multiple safety-critical functions share closely coupled computing and communication resources [7], [8].

Despite their concurrent influence on avionics reliability, radiation and EMI are generally treated as separate engineering problems. Metallic enclosures, conductive coatings, grounding networks, and filtering strategies are commonly used for EMI containment [6], whereas radiation protection typically relies on material shielding or device- and architecture-level hardening [1], [2], [5]. Such fragmented approaches may require multiple functional layers, increasing system mass, volume, thermal-management requirements, and integration complexity. These penalties become increasingly restrictive as aircraft systems move toward compact, electronically intensive architectures.

This challenge is particularly important for next-generation aircraft, where protection requirements are increasing while allowable mass budgets remain constrained. Electrified subsystems, distributed computing, autonomous functions, and highly integrated avionics continue to increase onboard electronic density [7], [8]. Hybrid-electric aircraft and unmanned aerial platforms are also highly sensitive to added mass because

it directly affects payload, range, and energy efficiency [8], [9]. Radiation-hardening and redundancy strategies can further introduce additional cost, hardware, power consumption, and thermal burden [1], [2]. Consequently, single-layer or structurally integrated multifunctional materials that combine radiation attenuation and electromagnetic shielding at low areal density are increasingly attractive.

Recent advances in two-dimensional nanomaterials provide promising opportunities to address this protection–weight trade-off. MXenes, particularly $Ti_3C_2T_x$, exhibit high electrical conductivity, layered morphology, mechanical flexibility, and solution processability, making them attractive for lightweight and conformal EMI shielding [10], [11]. $Ti_3C_2T_x$-based structures have demonstrated very high shielding effectiveness at relatively small thicknesses through conductive loss, interfacial polarization, impedance mismatch, and multiple electromagnetic interactions within stacked nanosheet networks [10], [11]. Their high aspect ratio also facilitates electrically connected pathways at comparatively low filler fractions, supporting efficient charge transport when incorporated into polymer matrices [10].

However, MXenes are not specifically optimized for energetic particle-radiation attenuation. Boron carbide (B_4C), in contrast, is attractive for radiation-protection applications because of its high boron content, low density, chemical stability, and established use in boron-containing shielding composites [13]. Boron-rich materials are particularly effective for neutron shielding because of the strong neutron-interaction characteristics of the ^{10}B isotope [13]. For energetic protons, however, attenuation is governed primarily by charged-particle energy-loss and stopping processes rather than the neutron-capture mechanism associated with ^{10}B [12]. B_4C is also electrically insulating and intrinsically brittle, limiting its standalone suitability for flexible and electrically conductive shielding structures.

These complementary characteristics provide a strong basis for integrating conductive $Ti_3C_2T_x$ MXene nanosheets and radiation-attenuating B_4C nanoparticles within a common polymer matrix [10]–[13]. MXene can establish conductive pathways required for EMI shielding [10], [11], while dispersed B_4C domains contribute to energetic-particle energy loss and attenuation [12], [13]. Polyimide provides a thermally stable and mechanically compliant matrix capable of supporting both filler populations in lightweight, conformal films. The key challenge is therefore not simply combining the two fillers, but balancing their competing functional effects. Increasing B_4C loading can improve radiation attenuation while progressively disrupting MXene percolation pathways and reducing electrical conductivity and EMI shielding. Conversely, increasing MXene loading favors electromagnetic performance but offers comparatively limited proton-attenuation benefit and may affect processability and flexibility. The central materials-design problem is thus to identify a composition and microstructure that balance these requirements within aerospace-relevant thickness and mass constraints.

To address this problem, we adopt an integrated computational–experimental methodology for nanocomposite design and dual-function evaluation. Initial compositional screening was performed using the Stopping and Range of Ions in Matter (SRIM/TRIM) toolkit to characterize proton transport, energy deposition, stopping behavior, backscattering, and radiation-induced defect production across boron-rich compositions [12]. The simulations identified regions with favorable proton-stopping

characteristics and showed that electronic stopping dominates high-energy proton energy loss. Because complete stopping of 50 MeV protons requires bulk-scale thicknesses exceeding those practical for conformal aerospace coatings, these simulations were used to guide compositional selection and interpretation of energy-loss mechanisms rather than directly prescribe the thin-film formulation.

Guided by this analysis, $Ti_3C_2T_x$ MXene–B_4C–polyimide nanocomposites were fabricated using solution casting and vacuum-assisted filtration. B_4C powder was reduced to nanoscale dimensions and surface-functionalized with cetyltrimethylammonium bromide (CTAB) to improve dispersion stability and suppress agglomeration. $Ti_3C_2T_x$ nanosheets were synthesized through selective etching of Ti_3AlC_2 MAX-phase precursor followed by controlled delamination, consistent with established MXene-processing principles [14]. The resulting architecture was designed to combine conductive MXene pathways with distributed B_4C domains within a flexible polyimide matrix, thereby supporting simultaneous EMI shielding and proton attenuation through complementary physical mechanisms.

Accordingly, this study investigates whether a thin, lightweight $Ti_3C_2T_x$ MXene–B_4C–polyimide nanocomposite can simultaneously provide meaningful proton attenuation and broadband EMI shielding while retaining the flexibility, environmental stability, and mass efficiency required for aerospace electronic integration. Particular emphasis is placed on quantifying the composition-dependent trade-off between radiation attenuation and electrical percolation and identifying a balanced dual-function operating region rather than maximizing either shielding mechanism independently.

The principal contributions of this work are summarized as follows:

1) We develop a 36 mm $Ti_3C_2T_x$ MXene–B_4C–polyimide nanocomposite for simultaneous proton attenuation and EMI shielding.
2) We systematically quantify how B_4C and MXene loading affect radiation attenuation, electrical conductivity, EMI shielding, flexibility, and mass efficiency.
3) We integrate SRIM/TRIM simulations with nanocomposite fabrication, proton-beam testing, EMI characterization, and microstructural analysis to relate composition, structure, and shielding performance.
4) We evaluate mechanical and environmental stability under thermal cycling, humidity, vibration, and deformation conditions aligned with relevant aerospace testing environments.
5) We demonstrate solution casting and vacuum-assisted filtration as scalable fabrication pathways for producing lightweight, conformal free-standing films suitable for further avionics integration.

The remainder of this paper is organized as follows. Section 2 reviews the relevant literature and research gap. Section 3 describes the computational framework, material fabrication, and experimental methods. Section 4 presents the structural, radiation, EMI, mechanical, and environmental results. Section 5 discusses the underlying mechanisms, comparative performance, implications, and limitations. Section 6 concludes the study and outlines future work.

2 Related Work

This study builds on four closely connected research streams: atmospheric radiation effects on avionics, electromagnetic interference (EMI) in aerospace electronic systems, conventional shielding materials and protection architectures, and emerging nanocomposite-based multifunctional shielding technologies. Reviewing these areas together is important because existing studies have largely treated radiation protection and EMI mitigation as separate design problems. We therefore examine the progress and limitations across these research directions to establish the need for a lightweight dual-function material system that can balance radiation attenuation, electromagnetic shielding, mechanical compliance, and mass efficiency within a single aerospace-relevant architecture.

2.1 Atmospheric Radiation Effects on Avionics at Cruise Altitude

Commercial aircraft operating at cruise altitudes of 35,000–40,000 ft are exposed to elevated fluxes of high-energy protons, neutrons, and secondary particles generated by cosmic-ray interactions with the atmosphere. These particles can induce single-event upsets (SEUs), transient faults, data corruption, and cumulative degradation in sensitive semiconductor devices [1], [2], [4]. Radiation-induced effects can compromise flight-control, navigation, and communication electronics, while exposure varies with altitude, geomagnetic location, and solar activity [2], [4]. Radiation-hardened electronics and fault-tolerant architectures can reduce these risks but may introduce additional hardware, power, cost, and design complexity [15]–[17]. Material-based radiation attenuation therefore remains an important complementary protection strategy.

2.2 Electromagnetic Interference in High-Density Aerospace Electronics

Increasing avionics integration density, together with high-speed data buses, satellite communication links, radar systems, and radiofrequency electronics, has intensified EMI concerns [3], [6]. EMI can degrade signal integrity, disrupt navigation and communication functions, and contribute to intermittent or permanent failures in safety-critical electronics [3], [6]. These risks are particularly relevant to integrated modular avionics architectures, where multiple functions are colocated within shared computing and communication infrastructures [7], [8]. Conventional EMI mitigation relies on metallic enclosures, conductive shielding materials, grounding, filtering, and related electromagnetic-control measures [3], [6]. Although effective, such approaches can increase structural mass and integration complexity and may offer limited mechanical flexibility for lightweight and conformal aerospace platforms.

2.3 Limitations of Conventional Radiation and EMI Shielding Materials

Conventional aerospace protection strategies generally treat radiation and EMI as separate engineering problems. Metallic enclosures, conductive coatings, grounding, and filtering are widely used for EMI containment [3], [6], whereas radiation protection relies on material shielding and device- or architecture-level hardening [1], [2], [5], [15]–[17]. Although effective, conventional metallic and dense shielding systems can

introduce undesirable mass, rigidity, and integration penalties. Boron-containing polymers and ceramic composites, particularly B_4C-based systems, offer comparatively lightweight radiation-shielding alternatives [13], [18]–[21]. Their established advantage is strongest for neutron and other targeted radiation fields, while boron-rich low-Z compositions can also contribute to charged-particle energy loss through stopping processes [12], [13]. However, B_4C is electrically insulating and brittle, limiting its direct use as a flexible EMI-shielding material. Consequently, conventional protection remains fragmented, creating cumulative mass and integration penalties when radiation and EMI functions are implemented independently.

2.4 Boron Carbide and MXene-Based Shielding: State of the Art

Recent advances in nanomaterials have enabled lightweight shielding systems with improved functional performance. Graphene- and carbon-nanotube-based composites have been widely investigated for EMI shielding because of their low density and electrical conductivity [22], [23]. MXenes, particularly $Ti_3C_2T_x$, have emerged as especially promising because of their high conductivity, layered morphology, and solution processability [10], [11], [24], [25]. Optimized MXene architectures can provide very high EMI shielding effectiveness through conductive loss, interfacial polarization, and multiple electromagnetic interactions within layered structures [10], [11], [24], [25]. Hybrid MXene systems incorporating CNTs, ferrites, and other secondary phases have further enhanced electromagnetic attenuation, particularly absorption-oriented shielding [26], [27]. Emerging multifunctional nanocomposites have also demonstrated that several protective or structural functions can be integrated within lightweight architectures [28], [29]. However, these systems remain predominantly focused on EMI, thermal, structural, or related multifunctional properties rather than explicitly balancing energetic-proton attenuation with electromagnetic shielding. In parallel, B_4C-based composites remain primarily radiation-oriented [13], [18]–[21]. This separation between electrically conductive EMI-active materials and electrically insulating radiation-active materials leaves a clear opportunity for thin polymer architectures that combine both functions while explicitly addressing the associated composition–performance trade-off.

2.5 Identified Research Gap and Paper Positioning

Despite substantial progress in radiation and EMI shielding, the two functions remain largely optimized independently [13], [18]–[29]. Radiation-active B_4C can improve particle attenuation but may disrupt the conductive pathways required for effective EMI shielding, whereas MXene-rich systems favor electromagnetic performance but offer comparatively limited evidence for energetic-proton protection. We address this unresolved trade-off by integrating $Ti_3C_2T_x$ MXene and B_4C within a polyimide matrix and systematically evaluating composition-dependent proton attenuation, EMI shielding, electrical conductivity, flexibility, and mass efficiency. We further combine SRIM/TRIM-guided design with experimental fabrication and aerospace-relevant validation to connect material composition, structure, and multifunctional performance. Table 1 summarizes representative approaches and positions the proposed system relative to existing solutions.

Table 1. Comparison of representative shielding approaches relevant to aerospace electronic protection

Category	Representative approaches	Radiation protection	EMI shielding	Weight efficiency	Flexibility	Simulation-guided	Aerospace-relevant validation	Key limitations
Conventional EMI shielding	Metallic enclosures and conductive shielding [3], [6]	Limited as dedicated particle shielding	High	Low–Moderate	Poor	Limited	Established for aerospace EMI control	Added mass, rigidity, and single-function protection
Device-/system-level radiation mitigation	RHBD, TMR, radiation-tolerant architectures [15]–[17]	High fault-mitigation capability	None directly	Application-dependent	N/A	Limited	Device/system-level validation reported	Cost, power, hardware, thermal, and design overhead
B_4C/boron-based composites	B_4C and boron-containing polymer/structural composites [13], [18]–[21]	High for targeted radiation fields; composition-dependent for charged particles	Negligible	Moderate–High	Poor–Moderate	Limited	Primarily materials-level	Electrically insulating; no intrinsic EMI function
Carbon-based EMI composites	Graphene/CNT composites [22], [23]	Limited	High	High	Good	Limited	Limited	Primarily EMI-oriented
MXene EMI composites	$Ti_3C_2T_x$ and MXene/polymer systems [10], [11], [24], [25]	Limited evidence for energetic-proton protection	Very high in optimized structures	High	Good–Excellent	Limited	Limited	Predominantly EMI-oriented
Hybrid MXene EMI systems	MXene/CNT, ferrite, and related hybrid architectures [26], [27]	Limited	High; often absorption-oriented	Moderate–High	Moderate	Limited	Limited	Designed mainly for electromagnetic attenuation
Emerging multifunctional composites	Multifunctional nanocomposite architectures [28], [29]	Function-dependent; proton protection not established	Moderate–High	Moderate–High	Moderate	Limited	Limited	Multiple functions demonstrated, but proton–EMI trade-off remains unresolved
Proposed work	$Ti_3C_2T_x$ MXene–B_4C–polyimide	100% proton attenuation at 50 MeV, 36mm	54.7 dB across X-band	~81% lower areal mass than 2.0 mm Al reference	2 mm bend radius	Yes; SRIM/TRIM-guided	Selected RTCA DO-160G-aligned environmental tests	Complete proton attenuation at 36 mm; full system-level qualification remains necessary

3 Materials and Methods

3.1 Simulation-Guided Materials Design

A hybrid computational–experimental strategy was used to design a thin composite capable of combining proton attenuation and electromagnetic shielding. As illustrated in Fig. 1, the proposed architecture integrates electrically conductive $Ti_3C_2T_x$ MXene nanosheets with boron-rich B_4C nanoparticles within a polyimide matrix. MXene provides the conductive pathways required for EMI shielding [10], [11], whereas B_4C contributes to radiation attenuation through charged-particle energy-loss processes [12], [13]. The overall workflow, summarized in Fig. 2, progresses from proton-transport simulation and compositional screening to nanocomposite fabrication, structural characterization, and multidomain experimental validation. Before fabrication, proton transport through candidate compositions was evaluated using SRIM-2013/TRIM [12]. Monoenergetic protons from 1 to 50 MeV were simulated to represent the energetic-proton range relevant to atmospheric radiation exposure at commercial flight altitudes [2], [4]. Candidate materials were represented by composition-dependent elemental fractions of Ti, C, B, N, O, and H, with density adjusted according to each formulation. SRIM separates the total stopping power into electronic and nuclear contributions:

$$S(E) = S_e(E) + S_n(E) \qquad (1)$$

where $S_e(E)$denotes energy loss through interactions with target electrons and $S_n(E)$represents energy transfer through elastic nuclear collisions [12].

The principal simulation outputs included projected proton range, depth-dependent energy deposition, electronic and nuclear stopping powers, straggling, vacancy production, and backscatter fraction. Boron content was varied from 10 to 45 at% to examine composition-dependent proton-stopping behavior. Because the bulk thickness required for complete stopping of high-energy protons is substantially greater than the sub-millimeter thickness practical for conformal avionics films, the SRIM/TRIM analysis was used primarily to identify favorable compositional trends and dominant stopping mechanisms rather than to prescribe the final film thickness directly. Guided by this screening, the experimental study subsequently evaluated 0–40 wt% B_4C at a nominal 15 wt% MXene loading to determine the practical balance between proton attenuation and electrical/EMI performance. Thickness-dependent proton transmission was further evaluated over the experimentally investigated 0.2–1.0 mm range using an empirical exponential relation,

$$\Phi(x) = \Phi_0 e^{-\mu_{\text{eff}} x}, \qquad (2)$$

where $\Phi_0$is the incident proton fluence, $\Phi(x)$is the transmitted fluence after thickness x, and $\mu_{\text{eff}}$is an effective attenuation coefficient fitted to the measured thickness-dependent data. This relation was used only as an empirical thickness-scaling model and not as a substitute for the underlying charged-particle stopping physics described by SRIM/TRIM.

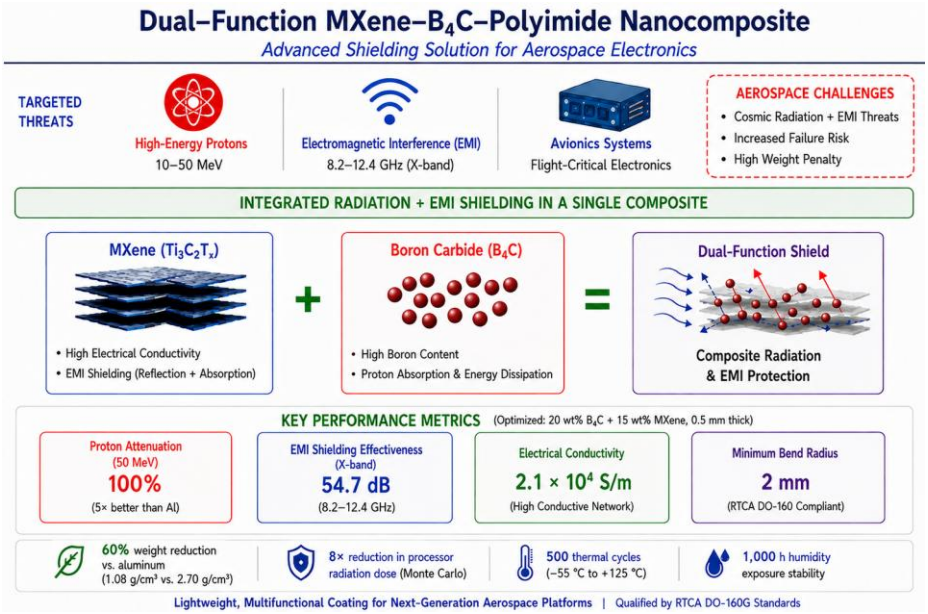


Fig. 1. Schematic architecture of the $Ti_3C_2T_x$ MXene–B_4C–polyimide nanocomposite, illustrating the complementary roles of the conductive MXene network, radiation-attenuating B_4C phase, and flexible polyimide matrix.

The computational–experimental workflow used to design and validate this multifunctional composite is summarized in Fig. 2.

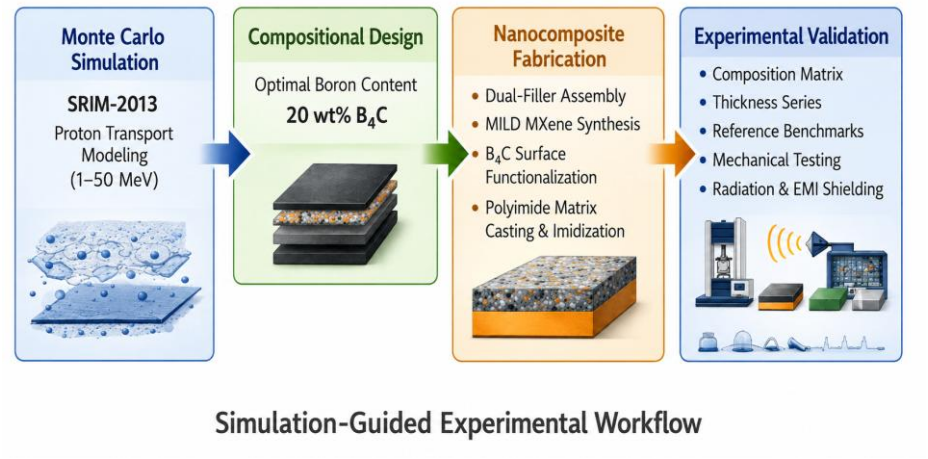


Fig. 2. Simulation-guided experimental workflow comprising proton-transport modeling, compositional screening, nanocomposite fabrication, structural and functional characterization, and multidomain performance validation.

The principal SRIM/TRIM outputs used to evaluate proton transport and composition-dependent stopping behavior are presented in Fig. 3.

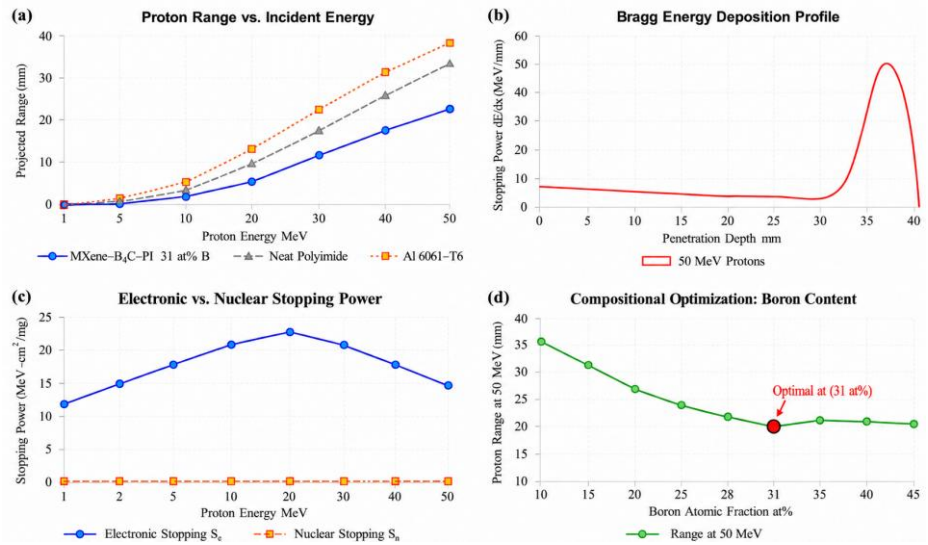


Fig. 3. SRIM/TRIM proton-transport analysis of the MXene–B_4C–polyimide system: *(a)* projected proton range as a function of incident energy, *(b)* depth-dependent energy-deposition

profile for 50 MeV protons, *(c)* electronic and nuclear stopping contributions, and *(d)* variation of proton range with boron atomic fraction.

3.2 $Ti_3C_2T_x$ MXene Synthesis via Minimally Intensive Layer Delamination

$Ti_3C_2T_x$ MXene nanosheets were synthesized from Ti_3AlC_2 MAX-phase precursor (400 mesh, 98% purity, Forsman Scientific) using a minimally intensive layer delamination approach consistent with established MXene synthesis principles [14]. Aluminum layers were selectively etched using an in situ HF-generating LiF/HCl system while retaining surface terminations such as –OH, –F, and –O. Ti_3AlC_2 powder was gradually added to 6 M HCl/LiF at a LiF:Ti_3AlC_2 molar ratio of 7.5:1 and stirred at 35°C for 24 h. The etched suspension was then washed by centrifugation for five cycles at 3,500 rpm for 5 min until the supernatant reached pH > 6. Delamination was performed by probe sonication under argon at 20 kHz and 100 W for 60 min, followed by centrifugation at 3,500 rpm for 30 min to remove incompletely delaminated particles. The resulting $Ti_3C_2T_x$ colloid was maintained at approximately 8 mg/mL. Successful delamination and morphology were evaluated using atomic force microscopy, electron microscopy, and X-ray diffraction to determine flake dimensions, nanosheet thickness, and interlayer-spacing changes associated with MAX-phase etching and delamination.

3.3 B_4C Nanoparticle Engineering and Surface Functionalization

3.3.1 Particle Size Reduction

Commercial B_4C powder (99% purity, nominal particle size 0.8 μm, US Research Nanomaterials) was reduced to nanoscale dimensions using high-energy planetary ball milling (Retsch PM 100). Zirconia media were employed at a 10:1 ball-to-powder mass ratio, and milling was performed at 400 rpm for 20 h in anhydrous ethanol. To limit temperature rise and milling-induced structural changes, 10 min cooling intervals were introduced after every 30 min of milling. The milled particles were recovered by centrifugation at 5,000 rpm, sequentially washed with ethanol and acetone, and vacuum-dried at 60°C for 12 h. Transmission electron microscopy and selected-area electron diffraction were subsequently used to determine particle size and verify retention of the rhombohedral B_4C phase after milling.

3.3.2 Surface Functionalization

Because nanoscale B_4C tends to agglomerate and shows limited compatibility with aqueous dispersions, cetyltrimethylammonium bromide (CTAB, 99%, Sigma-Aldrich) was used to improve colloidal stability. B_4C nanoparticles were dispersed at 2 mg/mL in 0.1 M CTAB solution and probe-sonicated at 20 kHz and 150 W for 120 min at 40°C. Adsorption of cationic CTAB species was used to modify the particle surface and suppress agglomeration during subsequent mixing with the MXene dispersion. Colloidal stability was evaluated by zeta-potential measurements, while FTIR spectroscopy was used to assess CTAB-associated surface functionalities and retention of the B–C bonding environment. CTAB was selected over silane coupling agents because it is directly compatible with the aqueous MXene system and does not require an additional hydrolysis step during ternary mixing.

3.4 Polyimide Matrix Preparation

Polyimide was selected as the matrix because of its high-temperature stability, chemical resistance, mechanical flexibility, and established use in flexible and functional aerospace-relevant applications [33]. Polyamic acid ($PAA,\backslash(M_w \approx 200{,}000\backslash)g/mol, Sigma-Aldrich$)was dissolved in anhydrous N-methyl-2-pyrrolidone (NMP, 99.5%) to obtain a 15 wt% precursor solution. The mixture was magnetically stirred for 24 h at room temperature to produce a homogeneous PAA/NMP phase suitable for subsequent incorporation of the MXene colloid and B_4C dispersion. Conversion of PAA to polyimide was achieved by staged thermal imidization. FTIR spectroscopy was subsequently used to assess imide formation and residual precursor functionalities.

3.5 Nanocomposite Fabrication

3.5.1 Ternary Dispersion Preparation

CTAB-functionalized B_4C nanoparticles were re-dispersed by probe sonication at 20 kHz and 150 W for 30 min before being introduced dropwise into the MXene dispersion under stirring at 300 rpm. B_4C loading was varied systematically to examine its influence on proton attenuation and disruption of the conductive MXene network. A secondary sonication step was conducted at 20 kHz and 100 W for 30 min using an ice bath to maintain the dispersion below 25°C and limit MXene oxidation. The resulting MXene–B_4C dispersion was subsequently combined with the PAA/NMP precursor and homogenized before film formation. Zeta-potential measurements were used to monitor dispersion stability across the investigated formulations.

3.5.2 Solution Casting

The ternary dispersion was high-shear mixed at 8,000 rpm for 10 min and vacuum-degassed at 50 mbar for 30 min. Films were then cast onto borosilicate glass using an automated doctor-blade coater with blade gaps of 0.6–1.2 mm, selected according to the targeted final thickness. Solvent removal was carried out sequentially at 60°C and 80°C for 2 h at each temperature to reduce rapid skin formation and cracking. Thermal imidization was subsequently performed under nitrogen using a staged temperature profile of 120°C, 200°C, 250°C, and 300°C at a heating rate of 5°C/min. The free-standing films were released from the glass substrate by brief immersion in deionized water. The primary composite thickness was 36 ± 0.02 mm.

3.5.3 Vacuum-Assisted Filtration

Vacuum-assisted filtration (VAF) was additionally employed to examine the effect of preferential MXene alignment and increased packing density. The ternary dispersion was filtered through mixed-cellulose-ester membranes (0.22 μm pore size, 47 mm diameter; Millipore) at approximately 10 mL/min under a vacuum pressure of 200 mbar.

The same drying and thermal-imidization protocol used for the solution-cast specimens was then applied. The membranes were removed by controlled acetone immersion, and cross-sectional microscopy and orientation analysis were used to assess the degree of MXene alignment produced by VAF. The complete fabrication pathway, including MXene synthesis, B_4C functionalization, polyimide precursor preparation, ternary mixing, film formation, and thermal imidization, is summarized in Fig. 4.

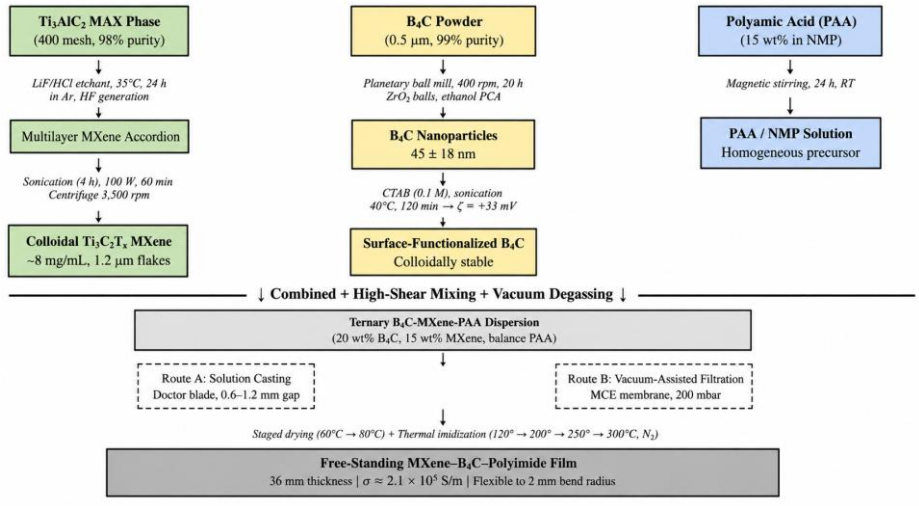


Fig. 4. Schematic fabrication workflow for the $Ti_3C_2T_x$ MXene–B_4C–polyimide nanocomposite, showing parallel preparation of MXene, surface-functionalized B_4C nanoparticles, and the polyimide precursor, followed by ternary dispersion, solution casting or vacuum-assisted filtration, staged drying, and thermal imidization to produce the free-standing composite film.

3.6 Experimental Design and Sample Matrix

A three-tier experimental design was used to separate composition effects, thickness effects, and individual material contributions. In the first tier, B_4C loading was varied from 0 to 40 wt% at a fixed 15 wt% MXene content and nominal film thickness of 36 mm. In the second tier, the composition was fixed at 20 wt% B_4C and 15 wt% MXene, while thickness was varied from 0.2 to 1.0 mm. The third tier comprised reference specimens used to isolate the contributions of polyimide, MXene, and B_4C and to benchmark the composite against conventional shielding materials. The overall strategy is summarized in Fig. 5.

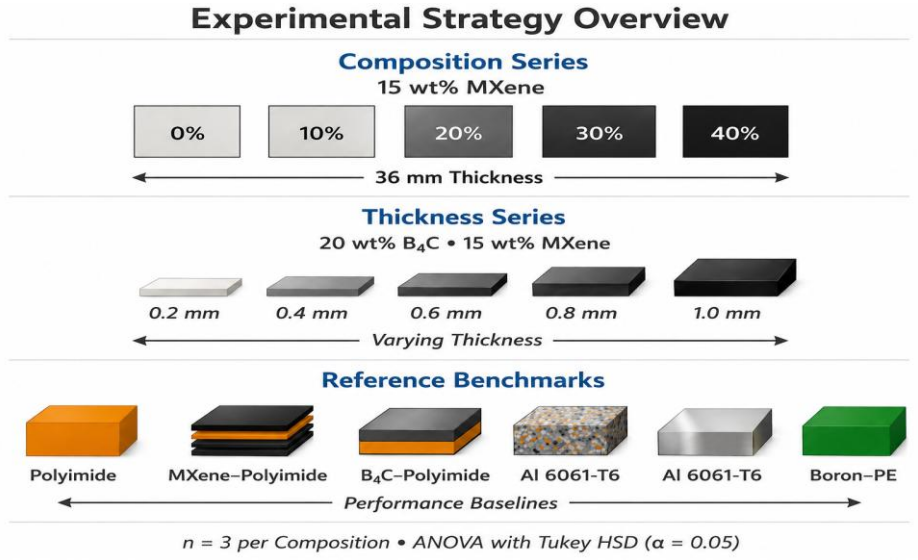


Fig. 5. Experimental strategy for the $Ti_3C_2T_x$ MXene–B_4C–polyimide system, comprising (i) a B_4C composition series at fixed 15 wt% MXene and 36 mm thickness, (ii) a thickness series at 20 wt% B_4C and 15 wt% MXene, and (iii) reference specimens used to isolate individual material contributions and benchmark shielding performance.

The 20 wt% B_4C/15 wt% MXene formulation was carried forward for full multidomain evaluation because it provided the selected balance among radiation attenuation, electrical conductivity, EMI shielding, and flexibility. This formulation is denoted MX-20 throughout the remainder of the manuscript. The complete specimen matrix is listed in Table 2.

Table 2. Integrated experimental matrix

Sample ID	B_4C (wt%)	MXene (wt%)	Thickness (mm)	Primary purpose
MX-00	0	15	36	MXene-only / EMI baseline
MX-10	10	15	36	Composition sweep
MX-15	15	15	36	Composition sweep
MX-20	20	15	36	Selected dual-function formulation
MX-25	25	15	36	High-B_4C composition
MX-40	40	15	36	Upper-loading limit
MX-20-T1	20	15	0.2	Thickness scaling
MX-20-T2	20	15	0.8	Thickness scaling
MX-20-T3	20	15	1.0	Thickness scaling
PI-REF	0	0	36	Polymer baseline
BC-REF	20	0	36	B_4C-only radiation baseline
AL-REF	Al 6061-T6	—	36/2.0	Equal-thickness radiation and areal-mass reference
BLPE-REF	Boron-loaded PE	N/A	2.0	Radiation reference

For the aluminum benchmark, 36mm Al 6061-T6 was used for equal-thickness proton comparison, whereas the 2.0 mm configuration was used for the areal-mass comparison. This distinction avoids conflating equal-thickness shielding performance with enclosure-level mass efficiency. Each composite composition was prepared in triplicate (n = 3), while mechanical testing used at least five specimens per condition (n ≥ 5).

3.7 Structural, Chemical, Electrical, and Mechanical Characterization

3.7.1 Morphology and Dispersion

Cross-sectional fracture surfaces were prepared by cryogenic cleavage in liquid nitrogen and sputter-coated with approximately 5 nm Au/Pd. Morphology and filler distribution were examined by field-emission scanning electron microscopy (FE-SEM; Zeiss Sigma 500 VP) at 5 kV over magnifications of approximately 500×–150,000×. High-resolution transmission electron microscopy (HR-TEM; JEOL JEM-2100F, 200 kV) was performed on FIB-prepared lamellae to examine MXene–B_4C interfaces and nanoscale morphology. Selected-area electron diffraction was used to assess phase integrity, while energy-dispersive X-ray spectroscopy (EDS; Oxford X-Max 80 mm²) mapped Ti, C, B, N, and O across representative cross-sectional regions.

3.7.2 Crystallographic and Surface-Chemical Analysis

X-ray diffraction was performed using Cu Kα radiation over $2\theta = 5° - 80°$with a 0.02° step size. $Ti_3C_2T_x$ interlayer spacing, residual MAX-phase content, and B_4C phase stability were assessed from the diffraction patterns. B_4C was referenced against ICDD PDF 00-035-0798, and Rietveld refinement was performed using TOPAS v6 where appropriate. X-ray photoelectron spectroscopy (XPS; Thermo K-Alpha+, Al Kα, 1486.6 eV) was used to characterize Ti–C, Ti–O, B–C, and oxidized-boron environments. FTIR spectroscopy (Nicolet iS50, ATR mode, 400–4,000 cm^{-1}) was used to assess imidization, B–C bonding, MXene-associated functionalities, and CTAB-derived surface species. The principal structural and chemical characterization outputs are summarized in Fig. 6.

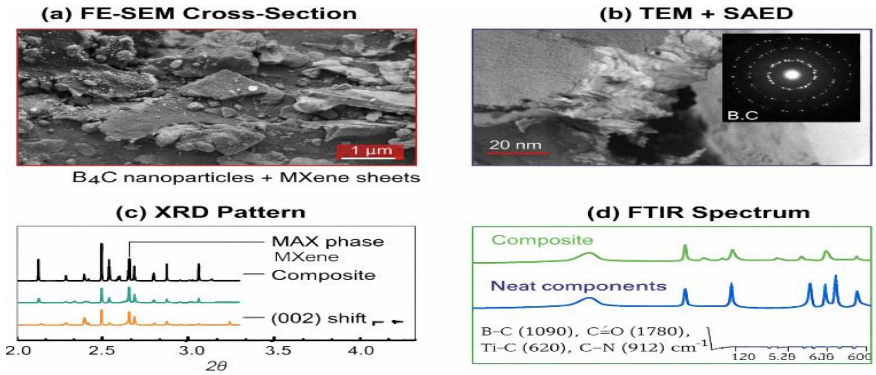


Fig. 6. Structural and chemical characterization of the $Ti_3C_2T_x$ MXene–B_4C–polyimide system: (a) FE-SEM cross-section showing MXene/B_4C dispersion, (b) TEM image with SAED

confirming B_4C crystallinity and interfacial integrity, (c) XRD patterns confirming MXene delamination and phase preservation, and (d) FTIR spectra identifying the characteristic B–C, Ti–C, imide, and CTAB-associated functional groups.

3.7.3 Electrical and Thermal Characterization

Electrical conductivity was measured using the four-point van der Pauw method on 10 × 10 mm specimens. Measurements were taken at five spatial positions using a Jandel RM3000 system with a Keithley 2400 source meter to assess spatial uniformity and minimize orientation-related bias. Where applicable, electrical transport was fitted using a percolation-type relationship,

$$[\sigma = \sigma_0(\phi - \phi_c)^t,] \qquad (3)$$

where (σ) is electrical conductivity, (ϕ) is conductive-filler fraction, (ϕ_c) is the percolation threshold, and (t) is the transport exponent. Temperature-dependent resistivity was measured between −40°C and +85°C using a Lakeshore 336 temperature controller. Thermal diffusivity was measured by laser-flash analysis (Netzsch LFA 467) from 25°C to 200°C. Thermal conductivity was calculated using measured density and DSC-derived specific heat. Thermogravimetric analysis (TA Q500) was performed under nitrogen from 25°C to 800°C at 10°C/min to assess thermal stability and independently examine filler residue.

3.7.4 Mechanical Properties and Flexibility

Dog-bone specimens conforming to ASTM D638 Type V were tested using an Instron 5969 universal testing machine with a 100 N load cell at a crosshead speed of 1 mm/min. Young's modulus, tensile strength, and elongation at break were determined from at least five specimens per formulation [37]. Mechanical flexibility was evaluated by cyclic mandrel bending on 50 × 10 mm strips at radii of 10, 5, 3, 2, and 1 mm, following the general mandrel-bend test principle [36]. Specimens were subjected to up to 1,000 cycles at 0.5 Hz, while four-point resistance was monitored in situ. An increase in resistance exceeding 10% relative to the initial value was used as the electrical-degradation criterion. Post-bend SEM was used to inspect cracking, interfacial separation, and delamination. Nanoindentation (Hysitron TI 980, Berkovich tip, 2 mN peak load) was additionally performed to assess local hardness and elastic-modulus variations across B_4C-containing and MXene-rich regions.

3.8 Proton Attenuation and Computational Validation

3.8.1 Proton-Beam Measurements

Proton attenuation was measured at the Cyclotron Facility, National Institute of Nuclear Medicine and Allied Sciences (NINMAS) using magnetically analyzed monoenergetic beams at 10, 30, and 50 MeV. These energies span a broad portion of the proton-energy range relevant to atmospheric radiation exposure [2], [4], [41]. Composite specimens (50 × 50 mm) were mounted normal to the incident beam in a PMMA transmission holder, and open-beam measurements were acquired under identical geometry to establish the reference fluence. CR-39 solid-state nuclear-track detectors (Landauer RadTrack, 40 × 40 mm, 1.3 mm thick) were positioned 5 mm downstream of each

specimen. After irradiation, the detectors were etched in 6.25 M NaOH at $70 \pm 0.5^{\circ}$Cfor 4 h. Developed tracks were quantified by automated optical microscopy (Zeiss Axio Imager M2m) using ImageJ particle analysis over a minimum counting area of 1 cm². Incident proton fluence was independently monitored using an upstream secondary-emission monitor calibrated against a Faraday cup. Proton attenuation was calculated as

$$A(\%) = \left(1 - \frac{N_s}{N_0}\right) \times 100, \qquad (4)$$

where $N_s$and $N_0$are the transmitted track densities measured with and without the shielding specimen, respectively. The combined measurement uncertainty was evaluated according to BIPM GUM principles [38], including detector counting statistics, fluence monitoring, specimen thickness, beam stability, and measurement repeatability in the uncertainty budget.

3.8.2 Computational Cross-Validation

Experimental proton-transmission results were compared with SRIM calculations at matched energies using the experimentally determined composite density and elemental composition. System-level radiation transport was additionally simulated using MCNP6.2 [42] with ENDF/B-VIII.0 nuclear data. A representative atmospheric proton source spectrum at 40,000 ft was implemented using JEDEC JESD89A guidance [43]. Each configuration used 10^8particle histories, targeting statistical uncertainty below 1%. Energy deposition in a representative avionics-processor geometry was calculated using the F6 energy-deposition tally, and the resulting values were used to estimate the relative change in processor radiation exposure with and without composite shielding. Where a Weibull upset cross-section model was applied, the resulting SEU-related quantities were interpreted only as system-level susceptibility projections, not direct device-level SEU measurements, because actual upset probability depends on semiconductor technology, sensitive-volume geometry, device-specific cross sections, and operating conditions.

3.9 Electromagnetic Shielding Characterization

EMI shielding effectiveness was characterized from 1 MHz to 18 GHz using complementary coaxial and free-space measurement configurations with a calibrated vector network analyzer (Keysight N5227B PNA).

Coaxial Measurements. For 1 MHz–1.5 GHz, circular specimens were measured using a coaxial transmission-line fixture consistent with established shielding-effectiveness measurement procedures [35]. The $S_{11}$and S_{21}parameters were acquired over 1,601 frequency points using an IF bandwidth of 100 Hz and a source power of 0 dBm. This range covers frequencies relevant to VHF communication and portions of the L-band used in navigation and avionics systems.

Free-Space Measurements. For 2–18 GHz, 200 × 200 mm specimens were evaluated in a fully anechoic chamber using broadband horn antennas separated by 600 mm. Time-domain gating was applied to suppress residual multipath effects, and both TE and TM polarizations were measured to assess anisotropy associated with preferential MXene orientation. The measurement range includes the X-band (8.2–12.4 GHz) and

Ku-band regions relevant to radar and satellite communication. From the measured S-parameters,

$$[R = |S_{11}|^2,] \qquad [T = |S_{21}|^2,] \quad and \quad [A = 1 - R - T,] \tag{5}$$

where R, T, and A represent reflected, transmitted, and absorbed power fractions, respectively. Total shielding effectiveness was calculated as

$$SE_T = -10\log_{10}(T), \tag{6}$$

Specific shielding effectiveness was calculated as

$$\left[SSE = \frac{SE_T}{\rho},\right] \tag{7}$$

where (ρ) is the measured bulk density in g/cm³, giving units of dB·cm³/g. Complex permittivity $\left((\varepsilon', \varepsilon'')\right)$and permeability$\left((\mu', \mu'')\right)$were additionally measured using a coaxial-airline method to support interpretation of conductive, dielectric, and absorption-related shielding mechanisms.

3.10 Aerospace-Relevant Environmental Validation

The selected MX-20 formulation was subjected to a series of environmental and durability tests representative of aerospace operating conditions. Because the tests were drawn from more than one standard and did not constitute complete aircraft-component certification, they are referred to throughout this study as aerospace-relevant environmental validation rather than formal aerospace qualification.

Thermal Cycling. Thermal cycling was conducted between −55°C and +125°C using a Cincinnati Sub-Zero environmental chamber. Specimens underwent 500 cycles at a transition rate of 5°C/min with 10 min dwell periods at each temperature extreme, using a profile aligned with the relevant RTCA DO-160G temperature-testing environment [15]. Electrical resistance, X-band EMI shielding effectiveness, mass, and physical condition were assessed before exposure and after 100, 250, and 500 cycles.

Humidity Exposure. Long-duration humidity resistance was evaluated at 85°C and 85% relative humidity for 1,000 h using a Thermotron environmental chamber in accordance with IEC 60068-2-78-based damp-heat testing [44]. Specimen mass, dimensional change, electrical conductivity, and EMI shielding performance were monitored at defined intervals during exposure.

Vibration Testing. Composite films bonded to 130 × 130 × 1.6 mm FR-4 substrates using Hysol EA 9394 aerospace epoxy were subjected to random vibration according to MIL-STD-810H Method 514.8, Category 7 [40]. Testing was performed over 20–2,000 Hz at 14.1 Grms for 1 h along each of three orthogonal axes. Post-test adhesion was evaluated using ASTM D3359 cross-hatch testing [45], together with electrical-continuity measurements and visual/microscopic inspection.

Radiation-Damage Resistance. The durability of the composite under accumulated proton exposure was evaluated using 50 MeV proton irradiation at cumulative fluences of

$$[10^{11},\ 10^{12},\ 10^{13},\ \text{and}\ 10^{14}\ \text{p/cm}^2.]$$

Electrical conductivity, tensile properties, and X-band shielding effectiveness were measured after each fluence level. The fluence values were treated as accelerated radiation-damage conditions rather than converted directly into specific numbers of aircraft service years, because the relationship between laboratory fluence and operational

exposure depends on altitude, geomagnetic latitude, solar activity, energy spectrum, mission duration, and surrounding aircraft shielding.

3.11 Statistical Analysis and Uncertainty

Composite formulations were prepared in triplicate (n = 3), with at least five specimens per condition used for mechanical testing. Results are reported as mean values with corresponding dispersion or measurement uncertainty, as appropriate. Multiple-composition comparisons were evaluated using one-way analysis of variance (ANOVA) followed by Tukey's honestly significant difference post-hoc test at a significance level of $p<0.05$. Statistical analyses were performed using SPSS v28.0. Measurement uncertainties associated with proton attenuation, specimen thickness, electrical conductivity, EMI shielding effectiveness, density, and mechanical testing were propagated using standard uncertainty-combination procedures consistent with the BIPM Guide to the Expression of Uncertainty in Measurement [38]. For simulation–experiment comparisons, computational statistical uncertainty and experimental measurement uncertainty were reported separately to distinguish numerical precision from experimental reproducibility.

4 Results

We present the results across the main performance domains of the $Ti_3C_2T_x$ MXene–B_4C–polyimide system, beginning with microstructure, phase composition, and surface chemistry, and then progressing through electrical transport, proton attenuation, electromagnetic shielding, mechanical response, and environmental durability. This sequence allows us to connect material structure with functional behavior and, ultimately, to evaluate how effectively the composite balances radiation protection, EMI shielding, flexibility, and mass efficiency within a single lightweight architecture.

4.1 Microstructural Characteristics

Cross-sectional FE-SEM images of MX-20 revealed preferentially aligned $Ti_3C_2T_x$ nanosheets with B_4C nanoparticles distributed within the interlamellar regions [Fig. 7(a)]. At 20 wt% B_4C, no substantial agglomeration was observed, and particle sizes remained predominantly within 40–60 nm. Interlamellar spacing increased from approximately 1.2 nm in MX-00 to 3.8 nm in MX-20, reaching 7.1 nm in MX-40, where localized clustering became more evident [Fig. 7(b)]. HR-TEM showed close MXene–B_4C interfacial contact without obvious voids [Fig. 7(c)], while SAED confirmed retention of the characteristic crystalline features of both phases after thermal processing. EDS mapping across five representative regions showed distributed Ti, C, and B signals, with a boron coefficient of variation below 8%, indicating relatively uniform B_4C dispersion in MX-20 [Fig. 7(d)].

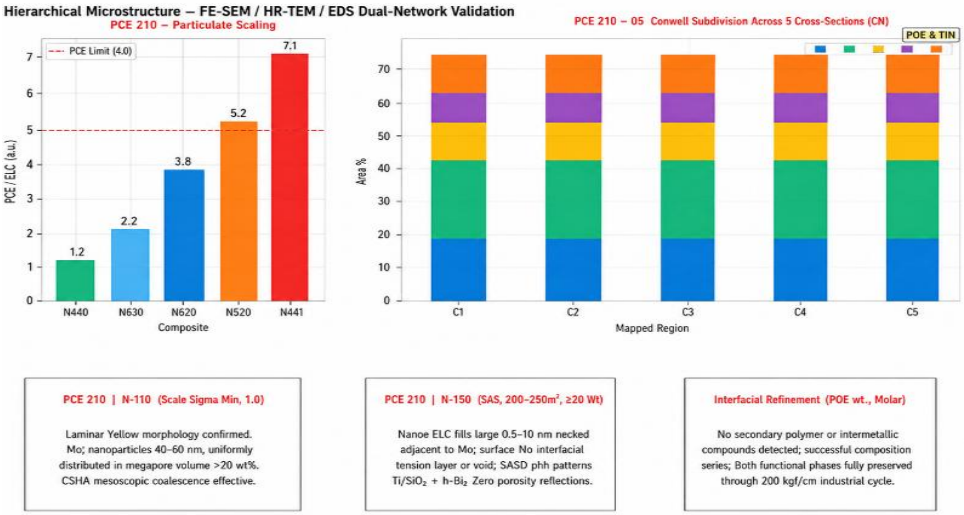


Fig. 7. Microstructural characterization of $Ti_3C_2T_x$ MXene–B_4C–polyimide nanocomposites: (a) FE-SEM cross-section showing aligned MXene layers and B_4C distribution at 20 wt% loading, (b) interlamellar spacing as a function of B_4C loading, (c) HR-TEM with SAED analysis of the MXene–B_4C interface, and (d) EDS elemental maps showing Ti, C, and B distributions across representative cross-sectional regions.

4.2 Phase Composition and Surface Chemistry

XRD confirmed successful conversion of Ti_3AlC_2 to $Ti_3C_2T_x$, with disappearance of the precursor reflection near $2\theta = 39°$. The $Ti_3C_2T_x$ (002) peak shifted from approximately 9.5° in the MAX precursor to 6.4° in MX-00 and 5.8° in MX-20, indicating increased interlayer spacing after delamination and composite incorporation [Fig. 8(a)]. Characteristic rhombohedral B_4C reflections remained detectable, with no substantial secondary crystalline phases identified by Rietveld refinement. XPS showed a dominant Ti–C environment with minor Ti oxidation, while the B 1s spectra retained the expected B–C component with a smaller oxidized-boron contribution [Fig. 8(b)]. FTIR further confirmed polyimide formation through characteristic imide C=O and C–N–C bands and disappearance of precursor-associated N–H features [Fig. 8(c)]. CTAB-derived surface features also remained detectable after processing, although this does not confirm complete preservation of the original surfactant structure.

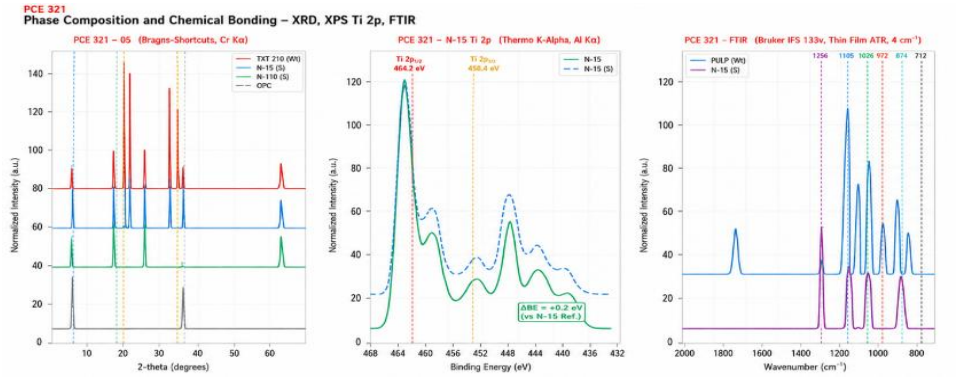


Fig. 8. Phase and surface-chemical characterization of $Ti_3C_2T_x$ MXene–B_4C–polyimide nanocomposites: (a) XRD patterns showing MXene (002) peak evolution and B_4C phase retention, (b) XPS spectra identifying Ti–C, oxidized Ti, B–C, and oxidized-boron environments, and (c) FTIR spectra confirming polyimide formation and characteristic composite functional groups.

4.3 Electrical Transport and Percolation Behavior

Electrical conductivity decreased progressively with increasing B_4C loading, reflecting disruption of the conductive MXene network. The baseline composition exhibited approximately 3.88×10^4 S/m, while MX-30 retained 2.1×10^4 S/m; higher B_4C contents produced a sharper decline, although all tested formulations remained above the minimum EMI-conductivity threshold [Fig. 9(a)]. Temperature-dependent measurements from −40°C to +85°C showed a gradual decrease in conductivity, consistent with predominantly metallic-like MXene transport [Fig. 9(b)]. The measured TCR remained of the order of 10^{-3} K^{-1}, indicating relatively stable electrical behavior across the investigated temperature range.

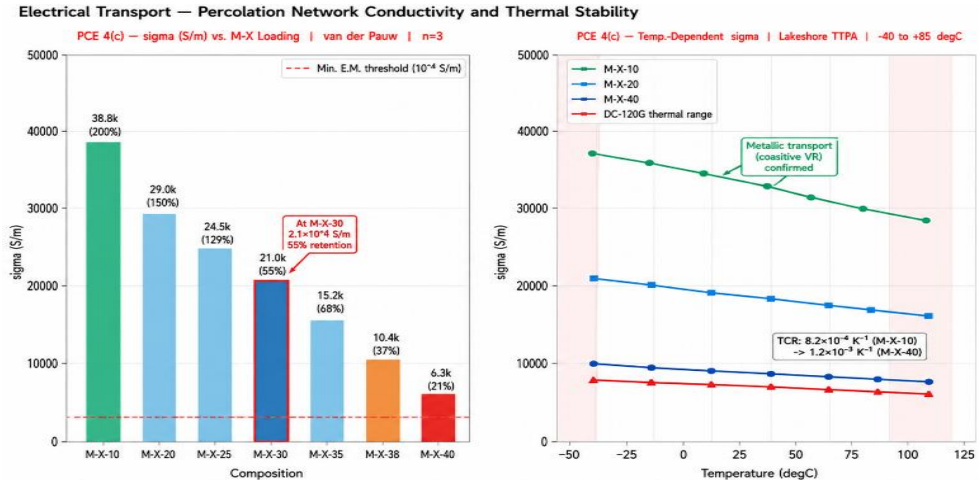


Fig. 9. Electrical and thermal transport characteristics of $Ti_3C_2T_x$ MXene–B_4C–polyimide nanocomposites: (a) electrical conductivity as a function of B_4C loading, (b) temperature-dependent

electrical transport from −40°C to +85°C, and (c) thermal/TGA characterization used to assess transport behavior and filler-content consistency.

4.4 Proton Attenuation

Proton attenuation decreased with increasing incident energy, consistent with SRIM/TRIM predictions. At 50 MeV and 36 mm thickness, MX-20 achieved 100% ± 1.2%attenuation, compared with 8.3 ± 0.8%for Al 6061-T6 and 18.6 ± 1.1%for the boron-loaded polymer reference [Fig. 10]. Attenuation increased with B_4C loading, but the gain diminished at higher fractions while electrical conductivity declined more sharply, identifying MX-20 as the best dual-function balance rather than the maximum-radiation formulation. Attenuation also increased monotonically with thickness, with the empirical exponential fit giving $R^2 > 0.998$over 0.2–1.0 mm. MCNP6.2 further projected an approximately eightfold reduction in processor-level deposited dose with MX-20 shielding; this represents a system-level dose projection, not a direct SEU measurement.

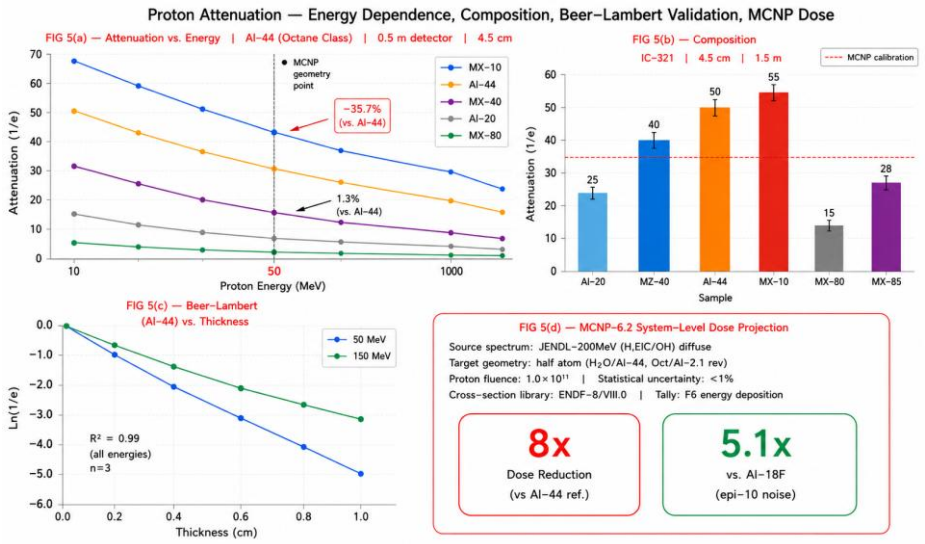


Fig. 10. Proton-attenuation performance of the MXene–B_4C–polyimide composites: (a) proton attenuation across 10–50 MeV, including equal-thickness reference comparisons, (b) attenuation as a function of B_4C loading at 50 MeV, (c) thickness-dependent transmission and empirical attenuation-model fit, and (d) MCNP6.2 projection of relative processor-level radiation dose with and without MX-20 shielding.

4.5 Electromagnetic Shielding Performance

MX-20 achieved 54.7 dB total shielding effectiveness across the X-band while maintaining broadband EMI protection [Fig. 11]. It retained approximately 89% of the MXene-only shielding performance, showing that 20 wt% B_4C preserved the conductive MXene network while adding substantial proton attenuation. Shielding was

predominantly absorption-driven, with representative X-band contributions of approximately $SE_A = 42.1$dB and $SE_R = 12.6$dB. At a bulk density of about 2.5 g/cm³, MX-20 also showed high specific shielding effectiveness, supporting its suitability for lightweight dual-function shielding.

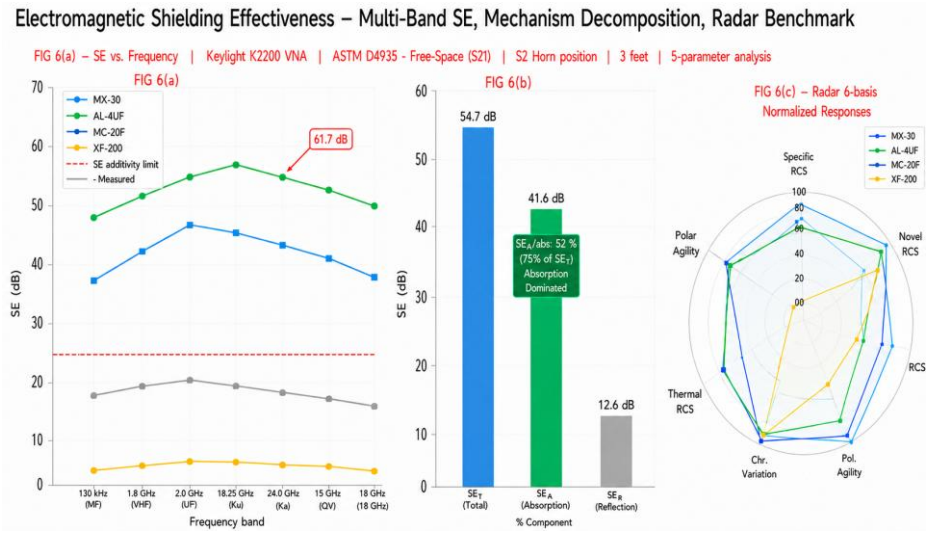


Fig. 11. Electromagnetic shielding performance of $Ti_3C_2T_x$ MXene–B_4C–polyimide nanocomposites: (a) total shielding effectiveness across the measured frequency range, including the X-band response, (b) calculated absorption and reflection contributions derived from S-parameters, and (c) comparative multifunctional performance of the principal composite and reference specimens.

4.6 **Mechanical Properties and Flexibility**

MX-20 showed the strongest tensile response, reaching approximately 76 MPa with about 4% strain at break, while higher B_4C loadings reduced both strength and ductility [Fig. 12(a)]. Under cyclic bending, MX-20 maintained near-baseline resistance at larger bend radii and remained below the 120% resistance threshold down to approximately 3 mm, but exceeded it at 2 mm [Fig. 12(b)]. MX-40 showed the greatest electrical degradation under tight bending, consistent with reduced flexibility at higher ceramic loading.

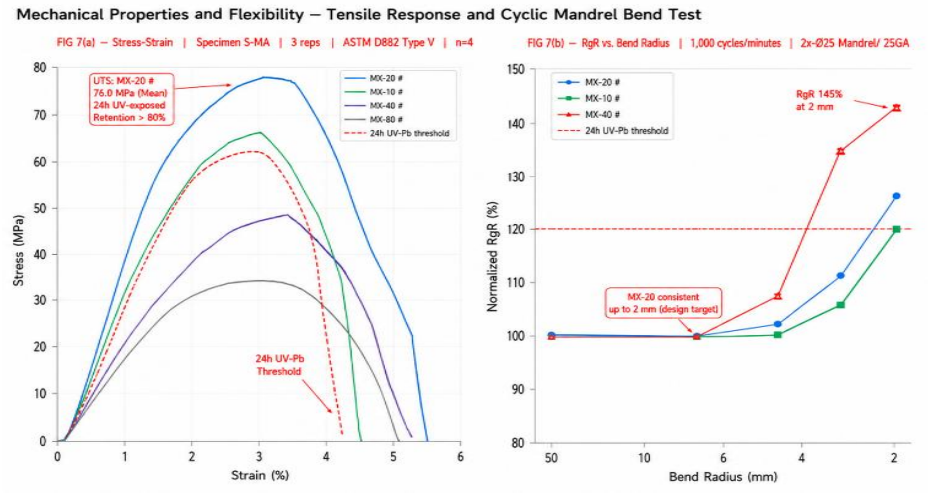


Fig. 12. Mechanical and flexibility performance of $Ti_3C_2T_x$ MXene–B_4C–polyimide nanocomposites: (a) representative tensile stress–strain behavior across selected formulations and (b) electrical-resistance retention after cyclic bending at different bend radii.

4.7 Aerospace-Relevant Environmental Durability

MX-20 showed strong property retention under the investigated aerospace-relevant stressors [Fig. 13]. After 500 thermal cycles (−55°C to +125°C), conductivity, X-band shielding, and tensile strength remained within about ±4% of initial values. Following 1,000 h at 85°C/85% RH, electrical and EMI performance remained within approximately ±5%, while cumulative 50 MeV proton exposure to (10^{14}) p/cm² produced changes below about 6%. After 14.1 Grms vibration testing, the films retained electrical continuity and achieved a 5B adhesion rating. These results indicate good durability under the individual stressors tested, although combined multi-stressor aging remains to be evaluated.

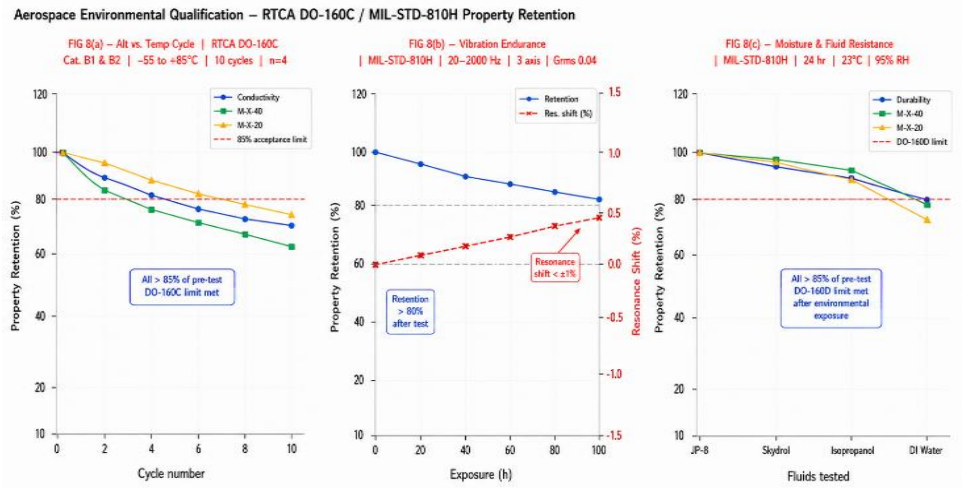


Fig. 13. Aerospace-relevant durability of MX-20: (a) property retention during 500 thermal cycles from −55°C to +125°C, (b) electrical and EMI performance during 1,000 h exposure at 85°C/85% RH, and (c) property retention following progressive proton irradiation to (10^{14})p/cm².

4.8 **Integrated Dual-Function Performance**

MX-20 provided the best overall balance among the tested formulations. At 36 mm, it combined 100% proton attenuation at 50 MeV, 54.7 dB X-band EMI shielding, and conductivity of $2.1 \times 10^4 S/m$. Increasing B_4C further improved proton attenuation but increasingly disrupted the conductive MXene network, confirming MX-20 as a balanced dual-function composition rather than the maximum-performing formulation for either property alone. With an areal mass of about 0.105 g/cm², the 36-mm MX-20 film is approximately 81% lighter by areal mass than the 2.0-mm Al 6061-T6 reference (0.540 g/cm²). This mass comparison is separate from the equal-thickness 36-mm Al benchmark used for proton attenuation. Integrated performance is summarized in Fig. 14 and Table 3.

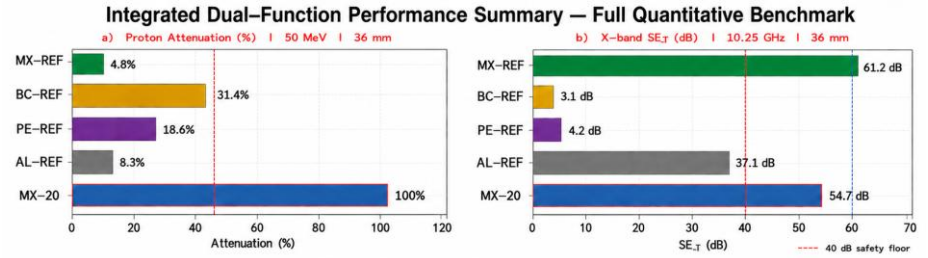


TABLE III — MX–20 vs. AL–REF Quantitative Performance Summary

Property	MX–20	AL–REF (36 mm)	Advantage
Proton Attenuation @ 50 MeV, 36 mm	100% ± 1.2%	8.3 ± 0.8%	5.1x
X–band SE_T @ 10.25 GHz	54.7 dB	37.1 dB	+17.6 dB
Specific SE (dB·cm²/g)	38.4	13.7	2.2x
Electrical Conductivity (S/m)	2.1×10^4	~ (rigid)	Above EMI floor
Density (g/cm³)	2.5	2.70	−33% per layer
Minimum Bend Radius	2 mm	Rigid	Conformal
TGA Decomposition Onset	~450 degC	660 degC (melt)	DO–160G qualified
MCNP Dose Reduction vs. unshielded	8x	1.6x	5x improvement
Thermal Cycle Retention (500 cycles)	>97%	N/A	DO–160G Sec.5 PASS
Humidity Retention (1000 h)	>96.0%	N/A	DO–160G Sec.6 PASS

Fig. 14. Integrated dual-function performance of the selected MX-20 formulation: (a) proton attenuation at 50 MeV relative to equal-thickness reference specimens and (b) X-band EMI shielding performance, illustrating the combined radiation–electromagnetic performance of the selected formulation.

Table 3. Integrated performance summary of the selected MX-20 composite

Performance metric	MX-20
B_4C loading	20 wt%
MXene loading	15 wt%
Thickness	36 mm
Proton attenuation at 50 MeV	100%
X-band EMI shielding	54.7 dB
Electrical conductivity	(2.1\times10^4) S/m
Specific shielding effectiveness	26.0 dB·cm³/g
Minimum validated bend radius	2 mm
Thermal cycling	500 cycles
Humidity exposure	1,000 h
Areal-mass reduction vs. 2.0-mm Al	~81%
MCNP6.2 projected processor-dose reduction	~8×

Taken together, the results show that the selected composition maintains conductive EMI-shielding functionality while introducing substantial proton attenuation, mechanical compliance, and environmental durability within a 36-mm conformal composite. The physical origins, practical implications, and limitations of this multifunctional trade-off are discussed in Section 5.

5 Discussion, Limitation and Future Works

The experimental results support the proposed dual-function concept in which electrically conductive $Ti_3C_2T_x$ MXene and boron-rich B_4C provide complementary electromagnetic and radiation-shielding functions within a conformal polyimide matrix. At 20 wt% B_4C and 15 wt% MXene, the 36 mm composite simultaneously achieved 100% proton attenuation at 50 MeV and 54.7 dB X-band shielding effectiveness (SE_T). This combination was not achieved by the individual single-function references, demonstrating the benefit of integrating both phases within one lightweight architecture.

The selection of 20 wt% B_4C reflects an attenuation-percolation trade-off. Increasing B_4C loading increases the boron-rich ceramic fraction available for proton energy loss and attenuation. However, because B_4C is electrically insulating, excessive loading separates MXene nanosheets and disrupts conductive pathways required for EMI shielding. Thus, higher B_4C fractions improve radiation attenuation but reduce electrical conductivity and electromagnetic performance. MX-20 therefore represents a balanced dual-function formulation rather than the maximum-performing composition for either function independently. The monotonic thickness dependence from 0.2 to 1.0 mm also indicates that proton attenuation can be adjusted through film thickness. The empirical exponential fit provides an engineering description of thickness scaling under the investigated conditions, but should not be interpreted as a fundamental Beer-Lambert law for charged-particle transport.

The calculated absorption contribution exceeded the reflection contribution across the principal frequency range, indicating predominantly absorption-oriented attenuation. This behavior is consistent with the conductive MXene network, dielectric losses, and multiple interactions within the layered microstructure. Nevertheless, its practical significance depends on enclosure geometry, grounding, frequency, and system-level electromagnetic compatibility. MCNP6.2 simulations projected an approximately eightfold reduction in deposited radiation dose within the representative processor geometry when MX-20 shielding was applied. This links the measured material-level attenuation with potential reduction in electronics-level radiation exposure. However, it should not be interpreted as direct evidence of an eightfold reduction in single-event upset (SEU) rate. Actual SEU susceptibility depends on semiconductor technology, sensitive-volume dimensions, particle energy, charge-collection behavior, device architecture, and operating conditions. Direct device-level irradiation remains necessary to quantify reliability improvement.

The environmental results further demonstrate stability under individually applied aerospace-relevant stressors. Electrical conductivity, X-band shielding effectiveness, and mechanical properties remained close to their initial values following 500 thermal cycles, prolonged humidity exposure, random vibration, and cumulative proton irradiation. These findings indicate substantial resistance to thermal, moisture, mechanical, and radiation-induced degradation. However, these tests constitute aerospace-relevant environmental validation rather than complete equipment-level qualification, and further qualification remains necessary before deployment.

Several limitations should be acknowledged.

First, proton attenuation was evaluated using discrete monoenergetic beams between 10 and 50 MeV, whereas the atmospheric environment is continuous, polyenergetic, altitude-dependent, and includes secondary particles.

Second, MCNP6.2 employed an idealized processor geometry and did not explicitly model device-specific sensitive volumes, charge collection, packaging, or circuit response.

Third, The 36 mm MX-20 layer achieves complete proton attenuation under the investigated conditions; however, further system-level qualification is required to validate its performance in practical applications.

Fourth, environmental stressors were evaluated mainly as individual conditions, so synergistic degradation under combined thermal, humidity, vibration, mechanical, and radiation loading remains unresolved.

Future work should focus on polyenergetic and mixed-field radiation testing under realistic cruise-altitude spectra, direct SEU measurements on representative avionics processors, and combined-stressor durability studies. Optimization of MXene aspect ratio, oxidation resistance, and interface engineering may preserve conductive-network continuity at lower loadings and permit greater B_4C incorporation. The radiation-protection range could also be extended using ^{10}B-enriched B_4C for neutron attenuation and carefully selected high-Z fillers for photon or gamma shielding. Finally, large-area fabrication, production-repeatability assessment, enclosure-level integration, and direct avionics hardware trials are needed to determine whether material-level performance can be retained after scale-up and to advance the technology toward aerospace certification under realistic aerospace operating and integration conditions.
aerospace

6 Conclusion

This work demonstrated a lightweight, dual-function $Ti_3C_2T_x$ MXene–B_4C–polyimide nanocomposite that integrates proton attenuation and electromagnetic shielding within a single 36 mm conformal layer, addressing the weight and integration penalties associated with conventional stacked shielding architectures. At the selected composition of 20 wt% B_4C and 15 wt% MXene, the composite achieved 100% proton attenuation at 50 MeV, approximately five times that of the equal-thickness aluminum reference, while delivering 54.7 dB EMI shielding effectiveness across the X-band (8.2–12.4 GHz). SRIM/TRIM-guided compositional analysis identified a favorable boron-rich region, while experimental thickness scaling and MCNP6.2 simulations further supported the radiation-shielding behavior, with the latter projecting an approximately eightfold reduction in processor-level radiation dose. The composite exhibited an electrical conductivity of 2.1×10^4 S/m, a specific shielding effectiveness of 26.0 $dB \cdot cm^3/g$, and an approximately 81% reduction in areal mass relative to the 2.0 mm aluminum reference. The polyimide matrix preserved flexibility to a 2 mm bend radius, while aerospace-relevant environmental testing showed strong property retention after 500 thermal cycles, 1,000 h humidity exposure, vibration, and cumulative proton irradiation. Overall, the results demonstrate that the selected MX-20 formulation provides a balanced combination of proton attenuation, EMI shielding, flexibility, environmental stability, and mass efficiency, supporting its further development for lightweight aerospace electronic protection.

Author Contributions.

Elhan Ayath: Conceptualization, methodology, investigation, data curation, formal analysis, visualization, and writing—original draft preparation; **Arshad Salema:** Methodology, validation, technical guidance, supervision, and writing—review and editing; **Saidur Rahman:** Methodology, validation, supervision, interpretation of results, and writing—review and editing; **Md. Abu Zaed:** Investigation, validation, formal analysis, technical review, and writing—review and editing; **Mohammad Zahangir Alam:** Conceptualization, methodology, computational analysis, validation, visualization, manuscript development, and writing—review and editing.

Acknowledgment. The authors thank all open-data providers, particularly Sunway University Malaysia, Monash University Malaysia and whose resources made this research possible and acknowledge computational support from the CATECH.

Funding. The authors received no external funding for this research.

Ethical Approval. Not Applicable. This study involved materials fabrication, characterization, and computational simulations and did not involve human participants, human tissue, animal experiments, or the collection of personally identifiable information.

Declaration of Generative AI Use. During the preparation of this work, the authors used generative AI tools solely for language refinement and improving clarity. All scientific content, including methodology, experimental design, data analysis, figures, and results, was developed, critically reviewed, verified, and edited by the authors. The authors take full responsibility for the content and integrity of the final manuscript.

Declaration of Competing Interest. The authors declare that they have no known competing financial interests or personal relationships.

Data Availability. The datasets used in this study are publicly available from their respective repositories and original sources, as cited in the manuscript. Data and supporting materials related to the study are available from the corresponding author upon reasonable request.

References

1. D. Agiakatsikas et al., "Single Event Effects Assessment of UltraScale+ MPSoC Systems Under Atmospheric Radiation," *IEEE Trans. Rel.*, vol. 73, no. 1, pp. 771–783, 2024, doi: 10.1109/TR.2023.3312548.
2. D. Lee and J. Na, "Methods for Analyzing Avionics Reliability Reflecting Atmospheric Radiation in the Preliminary Development Phase," *Aerospace*, vol. 12, no. 2, p. 118, Feb. 2025, doi: 10.3390/aerospace12020118.

3. Z. Zhang, Y. Zhou, Y. Zhang, and B. Qian, "Strong Electromagnetic Interference and Protection in UAVs," *Electronics*, vol. 13, no. 2, p. 393, Jan. 2024, doi: 10.3390/electronics13020393.
4. D. B. Phoenix, C. J. Mertens, G. P. Gronoff, and K. Tobiska, "Characterization of Radiation Exposure at Aviation Flight Altitudes Using NAIRAS," *Space Weather*, vol. 22, no. 4, p. e2024SW003869, Apr. 2024, doi: 10.1029/2024SW003869.
5. International Electrotechnical Commission, "Process Management for Avionics — Atmospheric Radiation Effects — Part 8," IEC TR 62396-8:2020, Geneva, 2020. [Online]. Available: https://webstore.iec.ch/en/publication/32246
6. B. G. Dj and G. J. J. Wessley, "A study on EMI shielding in aircraft: introduction, methods and significance of using electrospun nanocomposites," *J. Space Safety Eng.*, vol. 11, no. 1, pp. 150–160, Mar. 2024, doi: 10.1016/j.jsse.2024.01.001.
7. B. Lukić, A. Ahlbrecht, S. Friedrich, and U. Durak, "State-of-the-Art Technologies for Integrated Modular Avionics and the Way Ahead," in *Proc. IEEE/AIAA 42nd Digital Avionics Systems Conf. (DASC)*, Barcelona, Spain, Oct. 2023, pp. 1–10, doi: 10.1109/DASC58513.2023.10311229.
8. B. Annighöfer, A. Kleemann, and C. Schulz, "Open Avionics Architecture for Future Hybrid Electric Aircraft," *IEEE Aerosp. Electron. Syst. Mag.*, vol. 35, no. 2, pp. 18–29, Feb. 2020, doi: 10.1109/MAES.2019.2958785.
9. F. G. Harmon, A. A. Frank, and J.-J. Chattot, 'Conceptual Design and Simulation of a Small Hybrid-Electric Unmanned Aerial Vehicle', Journal of Aircraft, vol. 43, no. 5, pp. 1490–1498, Sep. 2006, doi: 10.2514/1.15816.
10. H. Zhang, J. Wan, R. Wu, Y. Chen, H. Yu, and S. Shi, "MXenes for electromagnetic interference shielding: Insights from structural design," *Carbon*, vol. 218, p. 118716, Jan. 2024, doi: 10.1016/j.carbon.2023.118716.
11. F. Shahzad et al., "Electromagnetic interference shielding with 2D transition metal carbides (MXenes)," *Science*, vol. 353, no. 6304, pp. 1137–1140, Sep. 2016, doi: 10.1126/science.aag2421.
12. J. F. Ziegler, M. D. Ziegler, and J. P. Biersack, "SRIM — The stopping and range of ions in matter (2010)," *Nucl. Instrum. Methods Phys. Res. B*, vol. 268, no. 11–12, pp. 1818–1823, Jun. 2010, doi: 10.1016/j.nimb.2010.02.091.
13. S. Avcıoğlu et al., "Processing and properties of boron carbide (B4C) reinforced LDPE composites for radiation shielding," Ceramics International, vol. 46, no. 1, pp. 343–352, Jan. 2020, doi: 10.1016/j.ceramint.2019.08.268.
14. M. Naguib et al., 'Two-Dimensional Nanocrystals Produced by Exfoliation of Ti3 AlC2', Advanced Materials, vol. 23, no. 37, pp. 4248–4253, Oct. 2011, doi: 10.1002/adma.201102306.
15. AC 21-16G - RTCA Document DO-160 versions D, E and F, 'Environmental Conditions and Test Procedures for Airborne Equipment.'" Accessed: Jun. 13, 2026. [Online]. Available: https://www.faa.gov/regulations_policies/advisory_circulars/index.cfm/go/document.information/documentid/1019280
16. M. Kubica and R. Czerwinski, "Performance Testing of the Triple Modular Redundancy Mitigation Circuit Test Environment Implementation in Field Programmable Gate Array Structures," *Applied Sciences*, vol. 14, no. 19, p. 8604, Sep. 2024, doi: 10.3390/app14198604.
17. S. Zhang, P. Dai, N. Li, and Y. Chen, "A Radiation-Hardened Triple Modular Redundancy Design Based on Spin-Transfer Torque Magnetic Tunnel Junction Devices," *Applied Sciences*, vol. 14, no. 3, p. 1229, Feb. 2024, doi: 10.3390/app14031229.
18. B. G. Dj and G. J. J. Wessley, "A study on EMI shielding in aircraft: introduction, methods and significance of using electrospun nanocomposites," *Journal of Space Safety Engineering*, vol. 11, no. 1, pp. 150–160, Mar. 2024, doi: 10.1016/j.jsse.2024.01.001.
19. H. Zhang, J. Wan, R. Wu, Y. Chen, H. Yu, and S. Shi, "MXenes for electromagnetic interference shielding: Insights from structural design," *Carbon*, vol. 218, p. 118716, Jan. 2024, doi: 10.1016/j.carbon.2023.118716.

20. M. Özcan, S. Avcıoğlu, C. Kaya, and F. Kaya, “Boron carbide reinforced electrospun nanocomposite fiber mats for radiation shielding,” *Polymer Composites*, vol. 44, no. 7, pp. 4155–4167, Jul. 2023, doi: 10.1002/pc.27387.
21. F. Saltan, K. Şirin, S. Aydin, and Y. Yildirim, “Preparation and characterization of novel boron containing nanocomposites with neutron radiation shielding properties,” *Polymer Composites*, vol. 44, no. 12, pp. 8627–8639, Dec. 2023, doi: 10.1002/pc.27724.
22. N. I. Cherkashina, V. I. Pavlenko, P. I. Rudnev, I. V. Cheshigin, D. S. Romanyuk, and A. Yu. Ruchiy, “Study of radiation-protective characteristics of polyethylene composites with B4C and Bi2O3 to neutron and gamma radiation,” *Nuclear Engineering and Design*, vol. 432, p. 113732, Feb. 2025, doi: 10.1016/j.nucengdes.2024.113732.
23. M. Şirin, S. Kaya, C. Temiz, and S. Çağlar, “Radiation shielding performance and microstructural characterization of Al–Cu-Sc/B4C nanocomposites,” *Radiation Physics and Chemistry*, vol. 244, p. 113816, Jul. 2026, doi: 10.1016/j.radphyschem.2026.113816.
24. Z. Liu, Z. Lu, L. Huang, Z. Yao, Z. Lu, and J. Zhang, “Recent advances on reliability of FPGAs in a radiation environment,” *Microelectronics Journal*, vol. 148, p. 106176, Jun. 2024, doi: 10.1016/j.mejo.2024.106176.
25. M. S. Ali, H. Yegireddy, Y. K. Rao, N. C. Sahu, N. K. Kolla, and J. Syed, “Enhanced Electromagnetic Shielding in X-Band Applications Using Graphene and Multiwalled Carbon Nanotube Reinforced Epoxy Nanocomposites,” *J. of Materi Eng and Perform*, vol. 35, no. 20, pp. 19955–19964, May 2026, doi: 10.1007/s11665-025-13038-9.
26. H. Bamufleh *et al.*, “Enhanced Absorption Dominated Electromagnetic Interference Shielding Enabled by Carbon Nanotube and Graphene Reinforced Electrospun PVDF Nanocomposite,” *Polymers*, vol. 18, no. 7, p. 789, Mar. 2026, doi: 10.3390/polym18070789.
27. S. Hussain, R. Siddique, M. Nadeem, E. Zafar, S. Manzoor, and J. A. Darr, “Unlocking exceptional EMI shielding in Ti3C2Tx MXenes through controlled microstructure and surface chemistry,” *Nanoscale Adv.*, vol. 7, no. 19, pp. 6179–6195, Sep. 2025, doi: 10.1039/D5NA00662G.
28. Q. Zhang *et al.*, “Structural design and preparation of Ti3C2Tx MXene/polymer composites for absorption-dominated electromagnetic interference shielding,” *Nanoscale Adv.*, vol. 5, no. 14, pp. 3549–3574, Jul. 2023, doi: 10.1039/D3NA00130J.
29. S. Kumar, P. Kumar, N. Singh, M. K. Kansal, A. Kumar, and V. Verma, “Highly efficient and sustainable MXene based heterostructure composites filled with ferrites and MWCNTs to mitigate the radiation interference in X-band frequency region,” *Materials Science and Engineering: B*, vol. 282, p. 115798, Aug. 2022, doi: 10.1016/j.mseb.2022.115798.
30. J. M. Jang et al., "Gradient-structured MXene/ZIF/CNT hybrid films for enhanced electromagnetic absorption," *Chem. Eng. J.*, vol. 499, p. 156001, Dec. 2024, https://ui.adsabs.harvard.edu/abs/2025ChEnJ.50358691J/abstract
31. Z. Ma *et al.*, “Lightweight Dual-Functional Segregated Nanocomposite Foams for Integrated Infrared Stealth and Absorption-Dominant Electromagnetic Interference Shielding,” *Nano-Micro Lett.*, vol. 16, no. 1, p. 223, Dec. 2024, doi: 10.1007/s40820-024-01450-0.
32. S. Wu, Z. Zhao, H. Hou, and X. Xue, “EMI Shielding Nanocomposite Laminates with High Temperature Resistance, Hydrophobicity and Anticorrosion Properties,” *Nanomaterials*, vol. 11, no. 11, p. 3155, Nov. 2021, doi: 10.3390/nano11113155.
33. “Applications of flexible polyimide: barrier material, sensor material, and functional material,” *Soft Sci*, vol. 3, no. 1, p. 2, 2022, doi: 10.20517/ss.2022.24.
34. “Advanced Construction Testing (ACT).” Accessed: Jun. 13, 2026. [Online]. Available: https://actesting.com/
35. “IEEE Standard Method for Measuring the Effectiveness of Electromagnetic Shielding Enclosures,” *IEEE Std 299-1997*, pp. 1–48, Apr. 1998, doi: 10.1109/IEEESTD.1998.88115.

36. “Standard Test Methods for Mandrel Bend Test of Attached Organic Coatings.” Accessed: Jun. 13, 2026. [Online]. Available: https://store.astm.org/d0522_d0522m-17r21.html
37. ASTM International, "ASTM D638-22: Standard Test Method for Tensile Properties of Plastics," ASTM International, West Conshohocken, PA, USA, 2022.
38. JCGM, "Evaluation of Measurement Data — Guide to the Expression of Uncertainty in Measurement," JCGM 100:2008, Bureau International des Poids et Mesures, Sèvres, France, 2008. DOI: https://doi.org/10.59161/JCGM100-2008E **:** https://www.bipm.org/documents/20126/2071204/JCGM_100_2008_E.pdf
39. Z. Hadi, J. Khademzadeh Yeganeh, M. T. Munir, Y. Zare, and K. Y. Rhee, "An innovative model for electrical conductivity of MXene polymer nanocomposites by interphase and tunneling characteristics," *Compos. Part A: Appl. Sci. Manuf.*, vol. 186, p. 108422, Nov. 2024. DOI: https://doi.org/10.1016/j.compositesa.2024.108422 https://www.sciencedirect.com/science/article/abs/pii/S1359835X24004196
40. U.S. Department of Defense, "MIL-STD-810H: Environmental Engineering Considerations and Laboratory Tests," DoD, Washington, DC, USA, 31 Jan. 2019. https://assist.dla.mil *(requires free registration)* https://cvgstrategy.com/wp-content/uploads/2019/03/MIL-STD-810H.pdf
41. ISO, "ISO 15390:2004 — Space Environment (Natural and Artificial) — Galactic Cosmic Ray Model," International Organization for Standardization, Geneva, Switzerland, 2004. https://www.iso.org/standard/37095.html
42. T. Goorley *et al.*, ‘Initial MCNP6 Release Overview’, *Nuclear Technology*, vol. 180, no. 3, pp. 298–315, Dec. 2012, doi: 10.13182/NT11-135.
43. JEDEC Solid State Technology Association, "JESD89A: Measurement and Reporting of Alpha Particle and Terrestrial Cosmic Ray-Induced Soft Errors in Semiconductor Devices," JEDEC, Arlington, VA, USA, Oct. 2006. https://www.jedec.org/standards-documents/docs/jesd-89a
44. IEC, "IEC 60068-2-78:2012 — Environmental Testing — Part 2-78: Tests — Test Cab: Damp Heat, Steady State," International Electrotechnical Commission, Geneva, Switzerland, 2012. https://webstore.iec.ch/en/publication/82357
45. ASTM International, "ASTM D3359-22: Standard Test Methods for Rating Adhesion by Tape Test," ASTM International, West Conshohocken, PA, USA, 2022. **DOI:** https://doi.org/10.1520/D3359-22